The Background: from Observation to a 'Non-Event' in Single-Crystal Diffractometry

Stefan T. Maes, Carine Vanhulle and Albert T. H. Lenstra*

*Department voor Structuurchemie, Antwerp University (UIA), Universiteitsplein 1, B-2610 Wilrijk, Belgium.
E-mail: lenstra@uia.ua.ac.be*

Abstract

The background–peak–background procedure is applied to calculate I and $\sigma^2(I)$ from diffractometer data. A standard measurement produces a raw intensity R and a local background B. This standard operating procedure results in $I = R - \gamma B$ and $\sigma^2(I) = \sigma^2(R) + \gamma^2\sigma^2(B)$, in which γ is the ratio of the times spent in measuring R and B. This approach has led to the conviction that the random error on I is determined by the signal and by the local background. Unfortunately, this concept is based on tradition. The strategic error in the background–peak–background routine is its complete neglect of the physical reality. Background intensities are produced by a single source, *viz* incoherent scattering. The relevant scattering processes are elastic (Rayleigh), inelastic (Compton) and pseudo-elastic (TDS) scattering. Their intensities are proportional to f^2, $(Z - f^2/Z)$ and $f^2[1 - \exp(-2Bs^2)]$, which results in a background intensity fully defined by θ only. With observed backgrounds available, a background model has been constructed with its proper mix of the three scattering processes mentioned. This model is practically error free because it is based on a signal with size $\sum B(H)$. The model-inferred background defines a zero level upon which the coherent Bragg intensities are superimposed. The distribution $P(R)$ of the raw intensity is given by the joint probability $P(I)P(B)$. $P(R)$ is known *via* the observation $R(H)$. The distribution $P(B)$ is a counting statistical one, for which the mean and the variance are available through the background model. So $P(I) = P(R)/P(B)$. This leads to $I = R - b$ and $\sigma^2(I) \approx I$. If serious attention is paid to the observed background intensities, the latter – ironically enough – ceases to be an important element in the random error $\sigma(I)$.

1. Introduction

Routinely, crystallographers rely on the background–peak–background (BPB) procedure to calculate the net intensity I from the original diffractometer data. In this routine, the local background B is subtracted from the raw intensity R. R and B are independently observed, which automatically leads to

$$I = R - \gamma B \qquad (1a)$$

$$\sigma^2(I) = \sigma^2(R) + \gamma^2\sigma^2(B). \qquad (1b)$$

γ represents the ratio of the times spent in measuring R and B. Exploiting the reflection profile, Lehmann & Larsen (1974) have introduced the concept of a γ optimization. French & Wilson (1978) have proposed a Bayesian analysis, in which negative intensities I can be avoided using a Wilson distribution as prior information. The separation of the elastic Bragg peak from its inelastic TDS companion has been discussed by Blessing (1989). In spite of these efforts, error analysis can hardly be regarded as a topic of major current interest in diffraction analysis. This is peculiar at the time that maximum-entropy methods are gaining momentum. They do so regardless of early warnings by *e.g.* Navaza (1991), who in his contribution to the Crystallographic Computing School at Bischenberg quoted Dante Alighieri: '*Lasciate ogni speranza voi chi entrate*'. Hell is present in a standard equation (de Vries *et al.*, 1994) of the type

$$\chi^2 = \sum_{II} \Delta^2/\sigma^2 = N,$$

which serves to constrain maximum-entropy calculations to the crystallographic reality of N observations.

In this paper, we will demonstrate that the random error σ obtained *via* (1b) is at best a zero-order approximation of the real error. *Sensu stricto*, equations (1a) and (1b) are only valid for a data set that is limited to one single observation of R and B. The application of the BPB procedure to a real crystallographic data set is common practice. In doing so, one prefers number crunching above strategy. This working practice conserves ignorance by cultivating complete neglect of experience and/or knowledge acquired during the preceding data collection. The fatal consequence of that unbalanced approach is the firm belief that $\sigma^2(I)$ depends on the signal and the background B [see (1b)].

Facts speak a different language. In a diffraction experiment, all observations $B(H)$ are interrelated. The background intensity is dictated by three scattering processes (James, 1967), *viz*:

(i) Elastic scattering. The Rayleigh intensity follows f^2.

(ii) Inelastic scattering. The Compton intensity is expressed by $(Z - f^2/Z)R^3$, in which Z is the atomic number of the scatterer and R^3 is a recoil factor.

(iii) Pseudo-elastic scattering. For an Einstein solid, the thermal diffuse scattering produces an intensity given by $f^2[1 - \exp(-2Bs^2)]$, in which B is the temperature factor of the scattering crystal (Willis & Pryor, 1975). This demonstrates that the scattering angle θ dictates for a given object its background signal.

In §2, we study the X-ray scattering by amorphous material. Lindemann glass served as source for incoherent scattering. A model description, which summarizes the experimental evidence, includes elastic and inelastic scattering. The crystalline contribution to the diffraction background is investigated in §3. Since the

(a)

(b)

Fig. 1. (a) Background intensities of amorphous glass: observation (▲), calculated with Rayleigh & Compton scattering (——) and calculated with a Debye slit function (- - - -) (see text). (b) Small-angle scattering for amorphous glass: observation (——). Calculated backgrounds are based on elastic and inelastic scattering with variations in the elastic component only: atomic Rayleight (▲), Debye slit correction (▼), radial distribution close packing 12-coordination (○) and 8-coordination (●).

intensity of the pseudo-elastic scattering depends on B(crystal), we included a temperature variation in our experiment. The model description is based on TDS and Compton scattering.

In §4, we divide the background intensity into its (pseudo-)elastic and inelastic components. This is possible by a combination of Mo $K\alpha$ radiation and an yttrium absorption foil ($\lambda_{abs} = 0.7276$ Å). The transmission through the foil shows a significant shift near $\theta = 36°$ due to the Compton shifted wavelengths.

Next we look at the impact of monochromator selection on the background. In §5, we compare graphite(002) and silicon(111). Coherent and incoherent scattering at the monochromator is analysed in §6.

In small $\sin\theta/\lambda$ intervals, the distribution of background intensities $B(H)$ matches a counting statistical distribution (Lenstra, Geise & Vanhouteghem, 1991). In cases with significant X-ray absorption, this equivalence is absent. In §7, the influence of absorption is analysed via an azimuth scan. It is shown that a transmission T for the coherent Bragg intensity changes into a transmission $T^{1/2}$ for the background. Therefore, an absorption effect on the primary diffractometer data is easily eliminated.

Crystal decay causes changes in coherent Bragg intensities as well as in the background. In §8, we discuss an example of this phenomenon. Here, the Bragg intensities go down in combination with a serious increase in background intensities for $\sin\theta/\lambda < 0.5$ Å^{-1}.

In §9, some technical aspects related to background intensities and aperture slits are discussed. Conclusions are drawn in §10.

2. The background generated by amorphous material

To increase the signal, we mounted a Lindemann-glass sphere with a diameter of 0.4 mm on our Enraf–Nonius CAD-4 diffractometer. A sealed Mo tube, operated at 20 mA and 50 kV, produced the incident X-ray beam, which was monochromatized by a pyrolitic graphite crystal (UCAR-ZYA) with a mosaicity of 0.4° full width at half-height in its rocking curve. The background was measured as a function of the scattering angle with the glass sphere in a fixed position. A stationary scan mode was applied. The angular resolution in the data collection was maximized by the insertion of a narrow optical slit (0.05 mm) in front of the detector. This slit defines the 2θ opening of the detector as 0.014°.

Measuring times were adjusted to the background signal and they reduce the counting statistical errors to values of 2% or better. The experimental results are depicted in Figs. 1(a) and (b).

The simplest model describing the background B_a of an amorphous material includes Rayleigh and Compton scattering. Equal weights should be assigned to both scattering processes because the incident beam determines the number of scattering atoms. Rayleigh scattering produces polarized radiation. Given the geometry
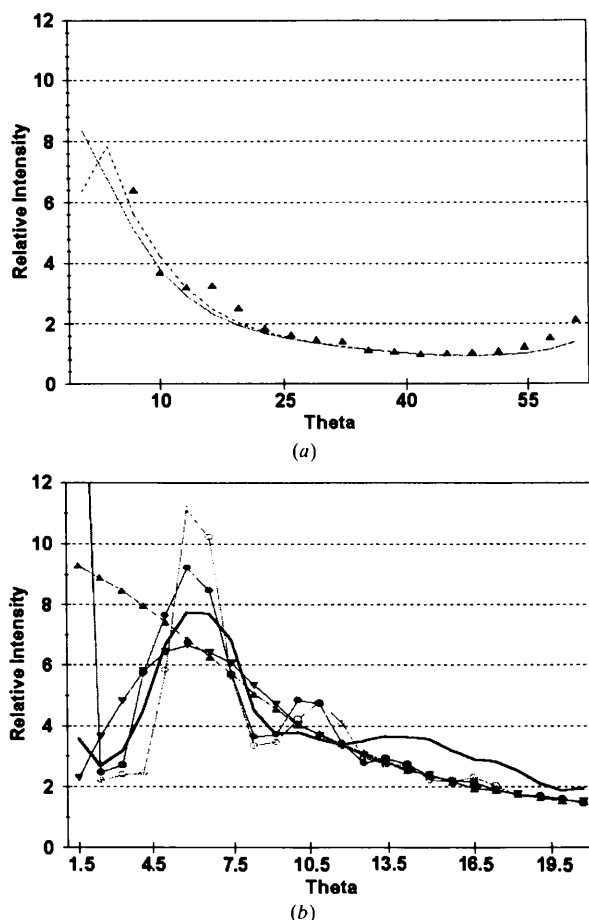
of our experimental arrangement, the polarization factor p is given by

$$\tfrac{1}{2}(\cos^2 2\theta_M + \cos^2 2\theta_D)$$

with θ_M the monochromator angle and $2\theta_D$ the scattering angle. For the Compton scattering, we found controversial opinions. Following Amorós & Amorós (1968, p. 373), the polarization of Rayleigh and Compton radiation is the same. This opinion is clearly not shared by Wooster (1962). The best fit between $B_a(\text{model})$ and $B_a(\text{observed})$ – see Fig. 1(b) – is obtained by following the opinion of Amorós & Amorós. Therefore, we will apply p from here on to all three scattering processes mentioned in the Introduction. Above $\sin\theta/\lambda = 0.5\ \text{Å}^{-1}$ ($\theta_D > 20°$), the agreement between model and experiment is satisfactory. The equation

$$B_a = p[f^2 + (Z - f^2/Z)R^3] \tag{2}$$

produces a valid fit with the measurements. Below $\sin\theta/\lambda \approx 0.5\ \text{Å}^{-1}$, we see serious discrepancies between model and reality. The model, which describes the elastic intensity via f^2, breaks down owing to its neglect of structural elements in the amorphous phase.

f^2 produces an adequate description for the Rayleigh intensity produced by a monoatomic gas at low pressure. Glass is hardly such a substance. An improved model is a noble gas under pressure. In that case, the elastic intensity B_R (James, 1967) can be rewritten as

$$B_R = f^2\big(1 - (\Omega/V)\{3[\sin(sd) - sd\cos(sd)]/(sd)^3\}\big), \tag{2a}$$

in which $s = 4\pi\sin\theta/\lambda$ and d is the van der Waals diameter of the noble-gas atom. The irradiated sample volume is V, whereas Ω is the volume occupied by the atoms in the sample. At low pressure, $\Omega/V \approx 0$ and thus $B_R = f^2$. A 'realistic' upper limit for Ω/V is 0.75, which is the volume fraction occupied by spherical atoms in a close-packed crystal lattice. The maximum in the background intensity at $\theta \approx 5.6°$ (see Fig. 1b) suggests a van der Waals diameter of 3.5 Å. We calculated the background intensity via (2), in which the atomic Rayleigh intensity f^2 was replaced by B_R [equation (2a)] with $d = 3.5$ Å and $\Omega/V = 0.75$. This is shown in Fig. 1(b). The introduction of a 'van der Waals' slit correction in the calculation of an elastic intensity is certainly an improvement. However, to go from a qualitative agreement to a more quantitative one requires additional information on the structural elements in glass. This is possible via changes in the interparticle distribution function $P(r_i - r_j)$. In (2a), we have $P(r_i - r_j) = 0$ if $|r_i - r_j| < d$ and $P(r_i - r_j)$ is a uniform distribution for $|r_i - r_j| > d$. A non-uniform distribution is better because it includes the number of nearest neighbours via a coordination model.

To analyse the impact of structure on the Rayleigh intensity, we decided to follow a small-angle-scattering approach. The elastic scattering of a molecule or an atomic cluster is given by

$$B(s) = \sum_{j=1}^{N} f_j^2 + \sum_{i=1}^{N}\sum_{j=1}^{N} f_i f_j \sin(r_{ij}s)/r_{ij}s, \tag{2b}$$

in which $s = 4\pi\sin\theta/\lambda$ and $r_{ij} = r_i - r_j$. The summation includes all N atoms in the molecule or cluster. The relevant expression for the background intensity is then given by

$$B_a = p[B(s) + N(Z - f^2/Z)R^3]. \tag{2c}$$

In a close packing, the reference atom is coordinated by 12 nearest neighbours. Using such a 13-atom cluster in (2b) with a nearest-neighbour distance of 4 Å produced a background profile (see Fig. 1b) with the same characteristics as the observed background intensities. Obviously, the model overestimates the real intensity at
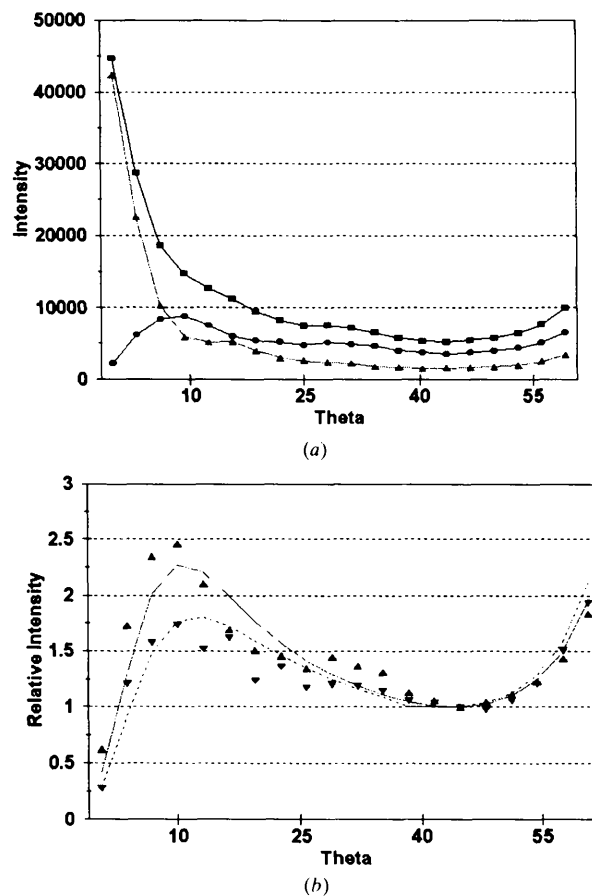

Fig. 2. (a) Background intensities at room temperature: observed for crystal and glass combined ($\blacksquare$), observed glass contribution ($\blacktriangle$) and difference background for the bithio crystal ($\bullet$). (b) Background intensities for the bithio crystal observed at 293 K ($\blacktriangle$) and 173 K ($\blacktriangledown$). Model intensites are (——) (293 K) and (- - - -) (173 K).

$\theta \approx 6°$. This is easily remedied by a reduction in the number of nearest neighbours, *i.e.* in the coordination number. We reduced the coordination number from 12 to 8 and recalculated *via* (2b) the background. The correspondence between experiment and model is in our opinion satisfactory. Further improvements require structural details like a B—O distance, which produces a background maximum around $\theta \approx 14°$ and the O···O distance ($\theta \approx 10°$) typical for an O—B—O valence angle.

3. The background produced by the crystal

To investigate the crystalline component in the total background intensity, we selected a single crystal of 1,2-bis(3-methoxy-2-thienyl)ethylene [bithio; space group *Pbca*; $a = 7.935$ (2), $b = 11.712$ (3) and $c = 13.217$ (2) Å; $Z = 4$; isotropic $B = 5.3$ Å^2 as the average B for all non-H atoms]. All $h00$ reflections ($-21 \leq h \leq 21$) were measured at three different azimuth angles ($-10, 0$ and $+10°$) in an $\omega/2\theta$ scan. The scan angle was given by $(1.3 + 0.7 \tan\theta)°$. The aperture was adjusted *via* $(2.7 + 0.4 \tan\theta)$ mm. A fixed scan speed of $0.4°$ min^{-1} was used.

As expected, the measurements were symmetric around $h = 0$. The variation in ψ had no significant impact on the observed data. The measurements were repeated in the absence of the bithio crystal. The results of these two room-temperature experiments are summarized in Fig. 2(a), which also shows the difference intensity, *i.e.* the crystalline component in the background. At higher θ values, we see that the glass capillary produces about 30% of the total background. The glass-related background in the region $0 \leq \theta \leq 20°$ differs considerably from the small-angle-scattering data shown in Fig. 1(b).

These differences are linked to:

(i) A considerable reduction in the amount of irradiated glass and the concomitant loss in signal size.

(ii) A large 'smearing' effect caused by the detector opening, which is roughly two magnitudes larger than the one used in the previous section. This smearing is enhanced by the integration over the scan angle, which is a common practice in step-scan measurements.

(iii) The presence of an adhesive used to fix the crystal to the capillary.

The glass-related background follows a pattern, which can be adequately described by our monoatomic background model [(2)]. This equation will be used in the subsequent sections.

To include the measuring procedure into the calculation of the theoretical background, we need to add a measurement correction M to the intensity expression. For a fixed scan speed, the time spent on the measurement is dictated by the scan angle $(a + b \tan\theta)$. A second correction takes care of the detector opening *via* its aperture $(c + d \tan\theta)$. This results in a correction M with

the form

$$M = [(a + b \tan\theta)/a][(c + d \tan\theta)/c].$$

The incoherent intensity B_c scattered by a crystal in the direction $s = \sin\theta/\lambda$ is given by

$$B_c = pM\{f^2[1 - \exp(-2Bs^2)] + (Z - f^2/Z)R^3\}, \quad (3)$$

in which B is the temperature factor of the crystal under investigation. Only the pseudo-elastic TDS intensity depends upon the temperature. The TDS intensity varies continuously with the scattering angle. Its maximum contribution to the background is usually found at $\theta \approx 10°$. This maximum is the consequence of the decrease in f^2 with increasing s and the opposite behaviour of $[1 - \exp(-2Bs^2)]$. The actual θ position of the maximum is directly related to the crystalline B (Willis & Pryor, 1975).

In Fig. 2(b), we compare B_c(model) with B_c(obs.). The maximum intensity B_c(obs.) is found at $\theta = 12°$, which points to an overall temperature factor of 5.5 Å^2 in the bithio structure. The correspondence with an average B_{iso} of 5.3 Å^2 – inferred from the net intensities *via* a normal structure determination – is gratifying.

To examine the temperature dependence of the TDS intensity, we repeated our experiments at 173 K. In a harmonic approximation, this reduces B from 5.5 to 3.2 Å^2. This leads to a reduction in the TDS intensity at low scattering angles. At high θ values, however, the TDS intensity reduces to f^2, which renders the background intensity as a temperature independent quantity.

B_c(model) is a reasonable summary of B_c(obs.) not only at 293 K but also at 173 K. However, there are discrepancies for scattering angles below 30°. The problems are related to two different elements, *viz* model simplicity and observational errors. Our current TDS description is attractive owing to its simplicity. It is also an approximation of a more complex reality. Strictly speaking, $f^2[1 - \exp(2Bs^2)]$ is tailored to a crystal with a single atom per unit cell. For a crystal structure with one molecule per unit cell, Amorós & Amorós (1968, ch. 3) rephrase the atomic formula into a molecular one: $I_{mol}[1 - \exp(-2Bs^2)]$. This leads to a local background at s that originates from a coherent scattering process for atoms within the molecule and an incoherent summation of molecular intensities over all unit cells. This approach successfully explains the presence of diffuse maxima in the background of molecular crystals. In our opinion, that structure-related TDS fine tuning introduces intensity fluctuations to be superimposed on a reference level dictated by $f^2[1 - \exp(-2Bs^2)]$. This view is not contradicted by the evidence given in Fig. 2(b).

An important error in our current analysis is the systematic discrepancy between the observed background and the real background. This lack in equivalence is the direct consequence of the wavelength dispersion. For an Mo tube in combination with a

graphite monochromator, we find $\Delta\lambda/\lambda$ values of 14% (Lenstra *et al.*, 1998). With $\lambda_{min} = 0.69$ and $\lambda_{max} = 0.79$ Å, the wavelength distribution in the incident beam is quite asymmetric with respect to the characteristic radiation with $\lambda = 0.71$ Å. This dispersion leads to a severe signal pollution in the background measurements. The coherent Si(0012) intensity at 0.75 Å is about 1% of the signal size at $\lambda = 0.71$ Å. This does not seem too important. However, when this small amount of coherent scattering is superimposed on the incoherent background, the observed background easily exceeds the real background signal by as much as a factor of 2. In our opinion, the wavelength dispersion errors are visibly present in Fig. 2(*b*). For $\sin\theta/\lambda \geq 0.7$ Å^{-1}, we have bithio intensities $I(h00)$, which are practically zero. So here systematic background errors caused by wavelength dispersion are absent. Model and observation

Fig. 3. (*a*) Mo $K\alpha$-induced background intensities of glass measured in the absence (■) and in the presence (▲) of an yttrium absorption foil in front of the detector. The variation in the transmission (- - - -) is caused by the Compton wavelength, which passes the Y-absorption edge at $\theta = 36°$. (*b*) Background intensity for glass and bithio crystal (——). The Y-related transmission (- - - -) was used to separate the background in an elastic (▲) and an inelastic (▼) component.

show a perfect fit. Below 0.7 Å^{-1}, we have $I(h00)$ with significant intensities and thus coherent scattering produces biased background intensities. It is here that model background and observation show the bulk of their discrepancies.

4. Elastic *versus* inelastic scattering

The Compton wavelength λ_c is related to the wavelength λ_i of the incident beam via

$$\lambda_c = \lambda_i + (h/mc)(1 - \cos 2\theta)$$

with $h/mc = 0.02426$ Å. So in an Mo $K\alpha$ ($\lambda = 0.7107$ Å) incident beam the Compton wavelength is 0.75 Å at a scattering angle θ of 65°. At $\theta = 36°$, λ_c passes the absorption edge of yttrium ($\lambda_{abs} = 0.7276$ Å). At that point, the linear absorption coefficient μ_Y shifts from 46.3 to 6.9 mm^{-1} for λ_c, which causes significant changes in the transmission of the background intensity. A typical example is shown in Fig. 3(*a*). With a Y foil between the scattering source and the detector, the observed transmission changes from 0.4 at low θ to 0.75 at $\theta \approx 60°$. As expected, the largest shifts in the transmission are found around $\theta = 36°$.

In a monochromatic environment, the transmission of 0.4 at, say, $\theta = 10°$ ought to be characteristic for λ_i. This is not the case. Stationary measurements at the position of the maximum intensity in the Bragg reflections produce a transmission of 0.36. In our opinion, this discrepancy of 10% between the transmissions in background and signal around $\theta = 10°$ reflects the lack of monochromaticity in the incident beam (*vide infra*). A transmission of 0.36 for $\lambda = 0.71$ Å produces a calculated thickness for the Y foil of 0.02 mm. This in turn leads to a theoretical transmission of 0.84 for $\lambda = 0.73$ Å. In the absence of a Y foil, the background intensity B_o is the simple sum of the elastic and pseudo-elastic intensity B_e and the inelastic Compton intensity B_c. In a simple approximation, the related intensity B_Y, observed *via* the yttrium absorption foil, is given by $0.36B_e + 0.84B_c$. This allows us to separate the original background into its elastic and inelastic components. An example of this reconstruction is shown in Fig. 3(*b*). At a scattering angle of 60°, the ratio between B_c and B_e is 8. This is practically equal to the theoretical ratio $(Z - f^2/Z)R^3/f^2$. So our current description for the background is adequate in terms of its balance between elastic and inelastic scattering. Moreover, a difference in polarization between elastic, pseudo-elastic and inelastic scattering would interfere with the B_c/B_e ratio. We find no indication for such a potential difference.

At low-θ angles, the calculated ratio between B_c and B_e is about 0.1. Clearly, B_c does represent a Compton intensity only for $\theta \geq 36°$. From the reflection profiles (see §5), the wavelengths present in the incident beam go from 0.69 up to 0.79 Å. So B_c for $\theta < 36°$ is indicative
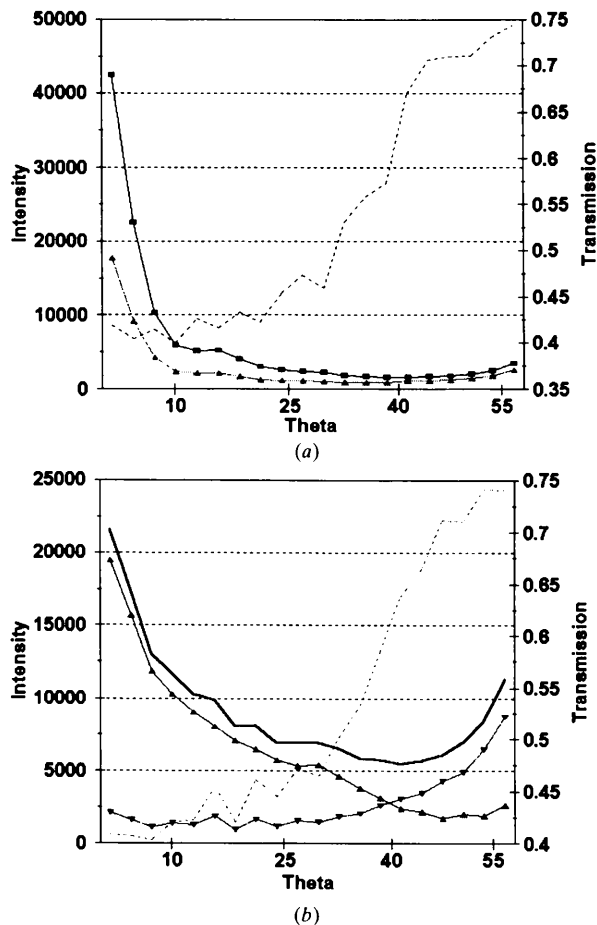
for the beam intensity linked to $\lambda > 0.7276$ Å. The observed ratio 0.1 between $I(\lambda > 0.73$ Å$)$ and $I(\lambda < 0.73$ Å$)$ suggests that the characteristic Mo $K\alpha$ radiation is responsible for only 90% of the incident beam.

This beam pollution is also visible in Fig. 3(b), in which every observation is linked to the reflection index h with $0 \leq h \leq 21$. For $h = 2n + 1$, we have $I = 0$. For $h = 2n$, we expect a reflection signal, in which the wavelength separation increases with the Bragg angle. For $5 \leq h \leq 11$, the observed transmission shows peculiar discontinuities in line with the reflection signal. On closer inspection we noted a transmission of 0.4 for the low-θ background and a transmission of 0.6 for the high-θ background of data with $h = 6, 8$ and 10. This is absent for $h = $ odd. In the data typical for amorphous material (Fig. 3a), the discontinuities are absent too. Here, wavelength dispersion due to Bragg scattering is non-existent.
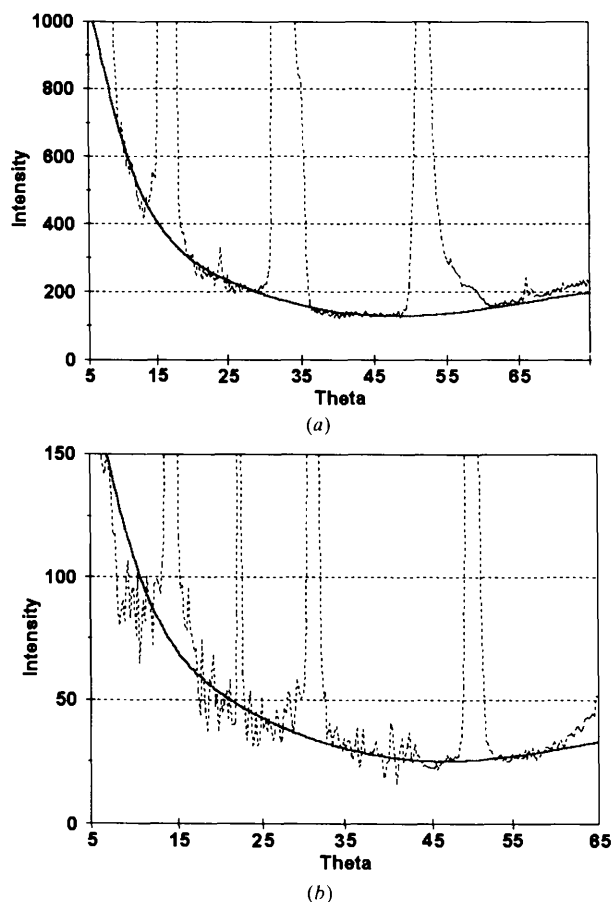

Fig. 4. (a) Intensity distribution along $\mathbf{c}^*$ for a silicon crystal. The incident beam is dictated by Mo $K\alpha$ radiation monochromatized via pyrolitic graphite. Calculated background intensities are marked by the solid line. The dashed line represents our observations. (b) As (a) but with an Si(111) crystal monochromator. Above $\theta = 60°$, the discrepancy between observation (- - - -) and model (——) is linked to radiation leakage at the monochromator.

Anomalous behaviour in the high-θ background of a reflection is linked to wavelengths longer than 0.7107 Å. Therefore, the evidence presented at $h = 6, 8$ and 10 confirms the skewness in the wavelength dispersion. This error also hampered our analysis of the crystalline background in §3.

5. The consequences of monochromator selection

For a given X-ray tube, the monochromaticity and the divergence of the incident X-ray beam are related to the mosaicity of the monochromator (Arndt & Wonacott, 1977). In the previous section, we already encountered problems related to the lack of monochromaticity. To avoid wavelength smearing by the crystal mounted on our CAD-4 diffractometer, we replaced the mosaic bithio crystal by a 'non-mosaic' silicon crystal with a size of $0.4 \times 0.4 \times 0.4$ mm. It had a rocking curve with a full width at half-height of 0.02°, which is a combination of its mosaicity and signal smearing by the 0.01° detector opening. The crystal itself was 'ideally imperfect', which we verified via its coherent Bragg intensities for data with $0 \leq h,k,l \leq 14$. We found I proportional to $f^2 \exp[-2Bs^2]$.

The incident X-ray beam was produced via a fine-focus Mo tube in combination with a graphite and a silicon monochromator. Monochromator angles are 6.1° for C(002) and 6.5° for Si(111). We measured intensities between 3 and 70° in scattering angle along the c^* direction of the analysing crystal. Intensity profiles of 004, 008 and 0,0,12 were measured using an $\omega/2\theta$ scan over a scan range of 21°. Each profile was dumped in 96 channels. Every scan was repeated at least 150 times. The averaged observed intensity pattern along $\mathbf{c}^*$ is shown in Figs. 4(a) (graphite) and (b) (silicon).

The width of the 0,0,12 reflection is about 3° in the Si(111)-dictated incident X-ray beam. The width increases to over 10° in the C(002)-controlled experiment. This points to a shift in wavelength dispersion from 0.03 to 0.14. The skewness of the 0,0,12 profile in the graphite-related X-ray beam is clearly visible. This skewness is incompatible with mosaicity as the driving force behind $\Delta\lambda/\lambda$. A detailed study on the monochromaticity will be presented in a forthcoming paper. Here it suffices to conclude that the success of background modelling will depend on our ability to control $\Delta\lambda/\lambda$.

In Fig. 4(a), we compare the experimental background with a model description as presented in §3. For the TDS contribution, we used $B(Si) = 0.5$ Å^2. Dividing our background intensity into an amorphous component B_a and a crystalline component B_c, we obtained a best fitting model which reads $B(\text{model}) = 4B_a + B_c$. The measure of fit R^2, defined as $\sum(B_{\text{obs}} - B_{\text{model}})^2 / \sum B_{\text{obs}}^2$ is 0.005 for background intensities with $8 \leq \theta \leq 65°$.

That same model, when applied to the Si(111)-related measurements, leads to an R^2 value of 0.046. Notably at

low-θ angles, the model seriously overestimates the observed background signals. The formula B(model) $= 2B_a + B_c$ produces the best fit with an R^2 value of 0.024. The reduction in B_a reflects in our opinion the beam divergence, which is minimal for the silicon mono-chromator. The models converged to relative r.m.s. residuals of 7 and 15% for graphite and silicon, respectively. The average background channel along $\mathbf{c}^*$ contains 200 counts for the graphite-related beam and 40 counts for the Si(111) dictated beam. So the r.m.s. residuals are in size equal to the counting statistical uncertainties in the two experimental analyses.

The measurements were repeated with a Y foil between the Si analysing crystal and the detector. The transmissions observed with the graphite mono-chromator are compatible with the evidence obtained with the bithio crystal. This is not the case with the results obtained with the Si(111) monochromator. The background transmissions around the 004 reflection were far too large.

The intensity of the incident beam produced via Si(111) is a magnitude smaller than the C(002)-dictated beam. This lowers the background signal to such small values that the detector noise level of 0.1 counts s^{-1} produces a detectable discrepancy between the observed background and the background signal. A zero-level compensation, based on the dark current of the detector, eliminated the anomalous behaviour in the Y transmission for $\theta_D < 45°$. Above 55°, we still found transmissions as if elastic scattering is non-existent. In Fig. 4(b), the anomalies coincide with the region $\theta > 55°$ where observation and model show increasing differ-ences. This discrepancy was caused by radiation leakage at the Si monochromator. A lead shield around the monochromator blocked the leaked radiation that reached the detector via the opening that serves to exchange attenuators. With the shield, the observed background falls in line with the calculated one.

Looking at Fig. 4(a), we note at high angles that B(obs.) $> B$(model). Radiation leakage, however, at the graphite monochromator does not exist. The same systematic difference between B(obs.) and B(model) is present in the amorphous background (see Fig. 2b). In our opinion, the most likely error source is a flaw in our calculation of the Compton intensity via $(Z - f^2/Z)R^3$. For oxygen at, say, $\theta = 70°$, the so-calculated incoherent intensity is about 5% less than the scattered intensity tabulated in International Tables for X-ray Crystal-lography (1968, Table 3.4.4.2B).

In the previous section, we found for a graphite-monochromated Mo beam a ratio between $I(\lambda > 0.73$ Å) and $I(\lambda < 0.73$ Å) of 0.1. This analysis supports that conclusion. The best wavelength separation is present in the Si(0,0,12) reflection profile (Fig. 4a). This allows an accurate split within the Si(0,0,12) signal at $\lambda = 0.73$ Å. The dividing line is not only easily calculated via $2d\sin\theta = \lambda$, but is also easily verified by a sudden

change in the Y transmission from 0.37 to 0.82 within the signal itself. We observed an $I(0,0,12)$ of 306 000 counts for $\lambda < 0.73$ Å in combination with an intensity of 34 000 counts for $\lambda > 0.73$ Å.

For the Si(0,0,12) in Fig. 4(b), i.e. using an Si(111)-monochromated beam, we find for $I(\lambda > 0.73$ Å) a zero intensity.

6. Coherent and incoherent scattering of the monochromator

To enumerate the crystalline contribution to the total background we used (3). Up to now, we used θ as a variable and λ was kept constant at the characteristic wavelength of the X-ray tube. The same expression, except for M, holds for monochromator scattering. With θ fixed and λ as a variable, (3) describes how the original tube spectrum is preserved in the incident X-ray beam via incoherent scattering.
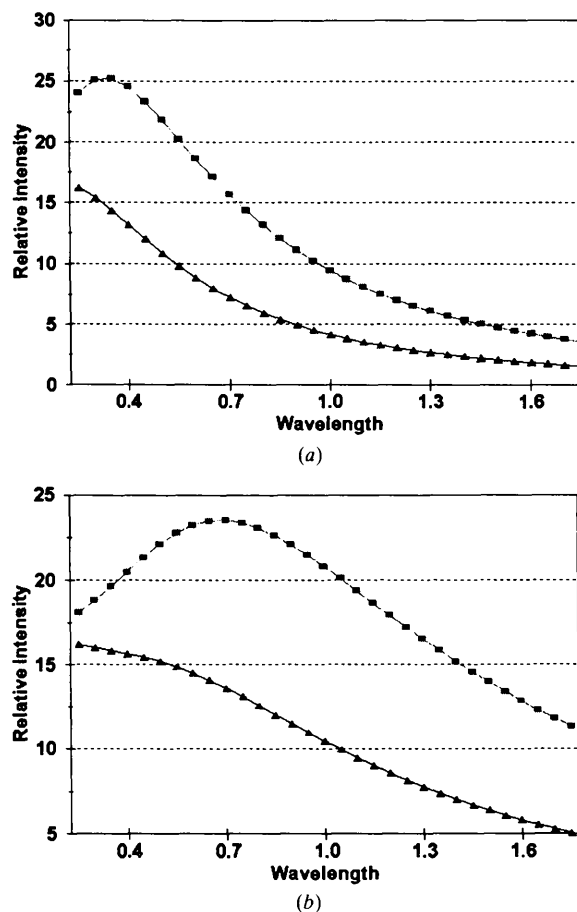

(a)

(b)

Fig. 5. Incoherent wavelength transmission via TDS and Compton scattering at the monochromator. (a) and (b) illustrate the difference for Mo ($\theta = 6.1°$) and Cu radiation ($\theta = 13.3°$) via the monochromator angle. Graphite (■) and silicon (▲) act differently because of the TDS component via B's set at 3.0 and 0.5 Å^2, respectively.

The minimum wavelength in the tube spectrum is dictated by the tube voltage V via $\lambda_{min} = 12400/V$ Å. At 50 kV, the minimum wavelength is 0.25 Å. Exploiting (3), we calculated the efficiency of incoherent wavelength transmission for $\lambda \geq \lambda_{min}$ for a silicon ($B = 0.5$ Å^2) and a graphite ($B = 3.0$ Å^2) monochromator. To simulate the difference between an Mo and a Cu geometry, we selected monochromator angles of 6 and 12°. The results are summarized in Figs. 5(a) and (b). Clearly, graphite is more efficient as a wavelength transmitter than silicon. This property is dictated by the temperature factor B, which suffices to explain the parallel behaviour in the intensity patterns of Fig. 5 and 2(b) via the relevant $\sin\theta/\lambda$.

Notably in the Mo geometry, short wavelengths are favoured above longer ones by the incoherent scattering process. Therefore, the incident X-ray beam will contain a deformed tube spectrum. This deformation will be enhanced by the monochromator absorption, which increases with increasing wavelength following an empirical relation (*International Tables for X-ray Crystallography*, 1967, p. 161):

$$\mu/\rho = C\lambda^3 - D\lambda^4.$$

The larger the absorption coefficient becomes, the smaller the intensity of the wavelength looked at will become, because μ determines the 'infinite thickness' of the monochromator and thus its scattering volume. This logic also explains the intensity difference in an Mo $K\alpha$ incident beam produced either by graphite or by silicon.

To measure, if possible, the wavelength pollution in the incident X-ray beam caused by incoherent scattering of the monochromator, we replaced on our diffractometer the Mo tube by an Rh tube ($\lambda = 0.6147$ Å). The diffractometer alignment was kept fixed to its original Mo geometry. The beam composition was analysed via
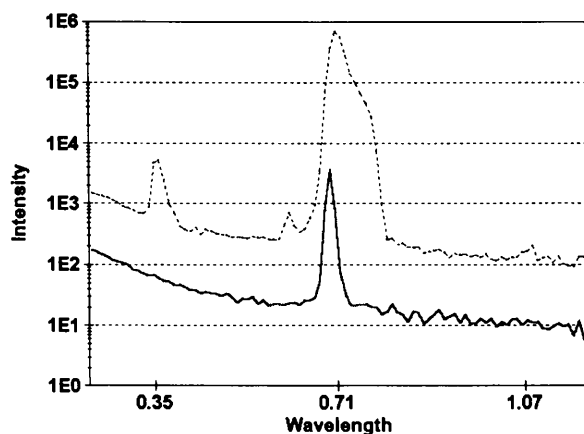

Fig. 6. Reflection profiles of Si(004) observed with graphite(002) (- - - -) and Si(111) (——) monochromators. Monochromator angles define coherent scattering for $\lambda = 0.71$ Å in the incident X-ray beam produced by a sealed Rh tube ($\lambda = 0.613$ Å).

the 004 reflection of the Si analysing crystal, which we observed in an $\omega/2\theta$ scan with a scan range of 21°. The intensity patterns, typical for a graphite- and a silicon-monochromated X-ray beam, are shown in Fig. 6.

In line with the diffractometer alignment, which gives coherent scattering for $\lambda = 0.71$ Å, we have in both profiles a strong (004) intensity at $\lambda = 0.71$ Å. The graphite monochromator produces also a small but significant signal for Si(004) at 0.61 Å. This Rh $K\alpha$ intensity is 0.1% of the intensity observed at $\lambda = 0.71$ Å. In the original tube spectrum – also observed via Si(004), but in the absence of a monochromator – the intensity for $\lambda = 0.71$ Å is only 2.5% of the intensity of the characteristic Rh $K\alpha$ radiation. So with the coherent intensity of 0.71 Å as reference, the incoherent scattering of graphite reduces the original Rh $K\alpha$ intensity by as much as 2×10^{-5}. This suffices to show that errors related to incoherent scattering at the monochromator will be less than 10^{-6} when the diffractometer is aligned in such a way that the characteristic radiation scatters in a coherent way.

The third maximum in the graphite-related intensity profile is either the 'forbidden' Si(002) reflection with $\lambda = 0.71$ Å or it is the Si(004) reflection with $\lambda = 0.355$ Å. The absence of Si(002) in the Si-monochromated profile points clearly at $\lambda = 0.355$ Å. $\lambda/2$ is present in the tube spectrum. It is coherently scattered as graphite (004). $\lambda/2$ cannot be coherently scattered via silicon because Si(222) is a 'forbidden' reflection with an almost zero intensity. The absence of $\lambda/3$ is in line with the applied tube voltage so that $\lambda/3 < \lambda_{min}$. Clearly, coherent scattering at the monochromator is much more important in wavelength pollution than incoherent scattering.

7. Background intensity and crystalline absorption

The distribution of experimental backgrounds $B(H)$ in small $\sin\theta/\lambda$ intervals has been shown (Lenstra, Geise & Vanhouteghem, 1991) to follow a counting statistical distribution. However, for crystals with a significant absorption, the observed backgrounds cannot be summarized in this way.

To analyse the impact of absorption, we used a single crystal of tetracopper tetraiodide thioamide (Maes *et al.*, 1998). The crystal size was 0.3 × 0.2 × 0.1 mm and its linear absorption coefficient $\mu = 13.4$ mm^{-1} for Mo $K\alpha$. The calculated transmission varies from 0.25 to 0.02 for an optical light path that shifts from 0.1 to 0.3 mm. The intensity variations in coherent and incoherent scattering were measured by rotation of the crystal around a reflection normal. The experiment is summarized in Fig. 7.

The intensity differences between equivalent measurements ($\Delta\psi = 180°$) are the results of X-ray absorption by the glass capillary. The background intensity and the Bragg intensity are strongly correlated

in terms of intensity gain and intensity loss. The ratios between the maximum signal ($\psi = 330°$) and the minimum signal ($\psi = 220°$) are 2 and 4 for background and signal, respectively.

The variation in Bragg intensity follows the Lambert–Beer expression

$$I = I_o \exp(-\mu l).$$

To calculate l (see e.g. the section on absorption in Ahmed, 1969), the experiment is represented in the standard sequence: light-source–sample–detector. In this setup, l depends on the incident-beam and scattered-beam directions. For the incoherent background intensity, the situation is different because light source and sample coincide.

If the incident beam and the scattered beam are equally important in the calculation of l for the signal, then the optical path relevant for the background is $l/2$. This leads to:

$$I/I_o = \exp(-\mu l) = T$$

$$B/B_o = \exp(-\mu l/2) = T^{1/2}$$

The simple logic links the variation in I to the one typical for B. Absorption programs eliminate the absorption errors from observed Bragg intensities. A small modification suffices to reconstruct 'absorption-free' background intensities.

8. Crystal decay and background intensities

A period of six months passed between our first and our last series of $h00$ measurements on the same bithio crystal. In that period, Bragg intensities decreased about 20%. Since reflection intensities are proportional to the volume of the crystal, we lost 20% of the original specimen. The background intensities for the two measurements mentioned are depicted in Fig. 8. For $\theta > 20°$, the observed backgrounds are practically identical. This means that the amount of scattering material did not change, which rules out sublimation as a possible driving force behind the signal loss.

At high θ angles, a transfer of molecules from the crystalline phase to an amorphous phase has no impact on the background because the Rayleigh intensity f^2 is equal to the TDS intensity $f^2[1 - \exp(-2Bs^2)]$ with $[1 - \exp(-2Bs^2)] \approx 1$. At low-$\theta$ angles, a transfer of molecules from the crystalline phase to an amorphous environment replaces $f^2[1 - \exp(-2Bs^2)]$ by f^2. Here, $f^2 > f^2[1 - \exp(-2Bs^2)]$ and thus we observe an increase in the background intensity.

To mount the bithio crystal on the glass capillary, we used a small amount of silicon paste P4 (Wacker Chemie). This combined with the experimental evidence points to the formation of a bithio solution in the silicon

paste. This is at the expense of the coherent Bragg scattering. The 200 reflection ($\theta \approx 5°$) goes down from 328 000 to 260 000 counts, whereas its background – corrected for our measurement with $\gamma = 2$ – increases from 38 000 to 58 000 counts. So the loss in signal and the gain in background are of the same magnitude. In our view, this is logical. For an average net intensity, we have $\langle I \rangle = \sum f^2 \exp(-2Bs^2)$. At $\theta = 5°$, $\exp[-2Bs^2] \approx 1$, so $\langle I \rangle \approx \sum f^2$. A transfer of material reduces this signal to $(1 - x)\sum f^2$ but it adds $x \sum f^2$ to the Rayleigh intensity.

9. Technical aspects in background measurements

All three background contributors vary continuously with the scattering angle. Small variations in the scattering direction, which are e.g. the consequence of the
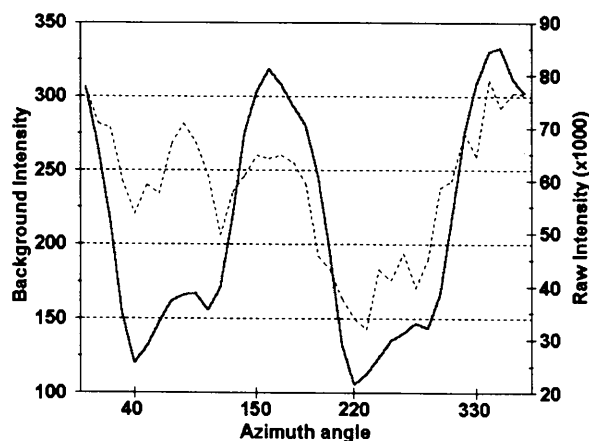

Fig. 7. ψ scan of the $1\bar{1}4$ reflection. The solid line indicates the raw intensity, the dotted line the background.
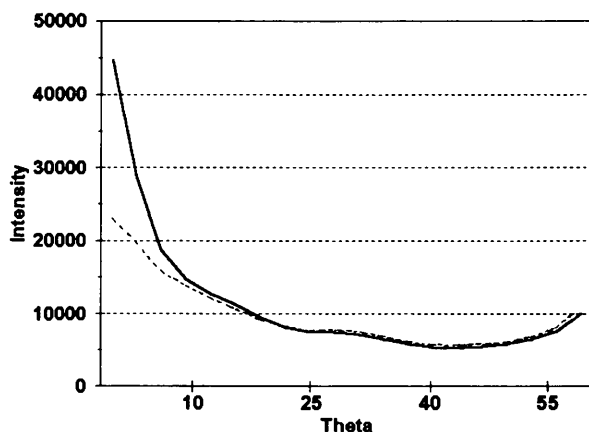

Fig. 8. Changes in background intensity due to crystal decay. Between the first measurement (- - - -) and the last measurement (——), a period of 6 months passed, in which the crystal dissolved slowly in the adhesive.

finite dimensions of the detector opening, have only a marginal influence on the scattered intensity. Therefore, the 'intense' incoherent scattering of the crystal produces an almost homogeneous illumination at the detector opening. Air scattering does the same but its image intensity is much weaker. Our observation is obviously the integrated total. This suffices to illustrate that background modelling does not require a homogeneous source of scattered light.

However, the incident X-ray beam should be homogenous in order to safeguard a constant irradiation during data collection. We tested the quality of the incident beam by mounting a small hole with a diameter of 25 μm at the crystal position on our diffractometer. This hole was translated in steps of 0.072 mm along the instrumental Y axis, which is parallel to the rotation axis of the monochromator. Over a distance of 0.5 mm, the intensities, observed with the detector fixed at $\theta = 0°$ and with a tube setting of 30 kV and 10 mA, were practically constant both for graphite as well as for silicon.

Shifts in the position of the hole along the direction of the wavelength dispersion of the monochromator revealed significant differences between the two monochromators. This is illustrated in Fig. 9. The graphite crystal produces an almost homogeneous beam, whereas the silicon monochromator shows an inhomogeneous beam with two intensity maxima separated by 0.4 mm. This distance is equal to the filament diameter of the Mo fine-focus tube. The silicon-related intensity profile reflects a form that matches with the mass projection of the filament on the anode. To verify this equality, we replaced the Mo fine-focus tube with its focal spot of 0.4 × 8 mm by an Mo broad-focus tube with its focus of 2.0 × 12 mm. For both tubes, the take-off angle was kept

Table 1. *Background intensity versus horizontal slit size*

Horizontal slit (mm)	Collimator 3 $\chi = 0°, \theta = 26°$	Relative intensity
1	2936	0.25
2	5663	0.48
3	8362	0.71
4	10526	0.89
6	11815	1

at 6°. The increase in filament diameter from 0.4 to 2.0 mm resulted in an improved beam homogeneity (see Fig. 9). Unfortunately, this improvement is at the expense of beam intensity.

The Mo fine-focus tube and the graphite monochromator produce an incident X-ray beam that is practically homogeneous over an area of 0.5 × 0.5 mm at the crystal position. The actual size depends on the selected collimator. In this standard experimental set-up, we analysed the influence of the optical slits on the background intensities.

The optical slits of the CAD-4 diffractometer are adjustable and they serve to optimize the signal-to-noise ratio. The collimator deals directly with the incident beam, which should have a diameter slightly larger than the crystal to be analysed. For the scattered beam, we have a double slit system, *viz*:

(i) the aperture, which defines the ω opening of the the detector *via* a vertical slit;

(ii) the manual slit, which limits the aperture to a finite vertical dimension.

In Table 1 and Table 2, we show typical results for background intensities as a function of the three slit systems mentioned above. It is clear that the background intensity increases with increasing pinhole diameter (beam width) and with increasing aperture. In §3, we assumed a linear relation between aperture slit and background intensity *via* the expression $(c + d \tan \theta)/c$. This is clearly a zero-order approximation because we see a non-linear relationship. A transformation from absolute intensities to relative intensities is very helpful. All aperture-related profiles reduce to a single reference profile. The relative intensities are linked to a normal distribution *via*

$$B = \int\limits_{-a}^{+a} \exp(x^2/2\sigma_{apt}^2) \, dx$$

with $\sigma_{apt} = 2.6$ mm and an actual aperture size of $2a$ mm. An analogous expression with $\sigma = 3$ mm holds for the manual slits. This non-linear relationship is in our view caused by the inconsistency between a rectangular detector opening and a circular scattering image produced by the scattering source and the beam tunnel. Aperture and manual slits act as curtains obscuring a circular light source.

The scattering volume of the crystal is a constant during data collection. This does not hold for the
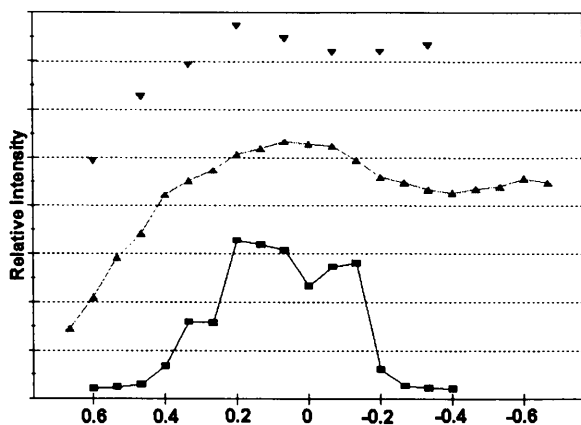

Fig. 9. Incident X-ray beam intensity distribution along the direction of the wavelength dispersion axis obtained by moving a 25 μm hole placed at the crystal position. The results shown apply to Mo fine-focus + Si(111) monochromator (■), Mo fine-focus + graphite monochromator (▲) and Mo broad-focus + Si(111) monochromator (▲).

Table 2. *Background intensity versus aperture/collimator size*

The X axis is in the incident-beam direction; the Z axis is perpendicular to detector plane.

| Aperture (mm) | Capillary // Y axis $\chi = 90°$ | | | Capillary // Z axis $\chi = 0°$ | | | | Relative intensity |
	Col. 3 $\theta = 26°$	Col. 1 $\theta = 26°$	Col. 2 $\theta = 26°$	Col. 3 $\theta = 26°$	Col. 3 $\theta = 13°$	Col. 3 $\theta = 52°$		
1.3	6306	2300	3213	3879	7871	2644		0.38
2	8961	3200	4452	5227	11027	3706		0.51
3	11376	4300	6059	7235	14792	4948		0.69
4	14458	5350	7630	9174	18971	6139		0.88
5	16118	5701	8305	9927	20585	6852		0.96
9	17359	5797	8313	10289	21406	7233		1

amount of irradiated glass used to mount the crystal. The amorphous contribution to the local background depends upon the Eulerian angles. At zero values for these angles, the capillary on our equipment is in a vertical position. A rotation around φ amounts to a translation of the capillary in a 'cylindrical' beam. This produces a scattering length l, which follows the equation

$$l^2 = r^2 - \varepsilon_{max}^2 \cos^2(\varphi - \varphi_o),$$

where r is the beam diameter and ε_{max} is the radius of the circular movement of the capillary. The angle ζ between the incident X-ray beam and the capillary is given by $\cos \zeta = \sin \omega \sin \chi$. The irradiated part of the capillary changes with $(\cos \zeta)^{-1}$.

10. Conclusions

In the previous sections, we were able to summarize our background intensities in a physical model. Absorption errors were shown to pose no serious problems because they can be corrected quite easily. The model proved to be flexible enough to deal with beam divergence, monochromator selection and measuring temperature. The balance between inelastic Compton scattering and (pseudo-)elastic scattering was properly struck.

The background expression is given by

$$B(\text{relative}) = t[d + p(\alpha B_a + B_c)M], \tag{4}$$

where t is the measuring time, d is the detector noise, p is the polarization factor and α is a weight factor to be used to equilibrate the scattering B_a of the amorphous material with the crystalline scattering B_c. B_a and B_c were both expressed in terms of an individual atomic scatterer. This simplicity makes the background description extremely useful because it does not require any specific structural information. This allows the construction of a background model prior to the actual structure analysis.

An alternative for the physical description of the background exists in the form of an anonymous background analysis. A demonstration of this approach has been published by Eisenstein & Hirshfeld (1983). They used a function of the type

$$B(\theta, \chi, \varphi) = B_o B_\theta(\theta) B_\chi(\chi) B_\varphi(\varphi),$$

where θ, χ and φ are the Eulerian angles of the diffractometer. B_θ and B_χ are polynomials in θ and χ, respectively, whereas B_φ is a polynomial in $\cos(\varphi - \varphi_o)$.

The background model – physical or anonymous – combines all measurements $B(H)$ into a new instrument. This tool is based on a signal with the size of $\sum B(H)$. Therefore, the model accuracy is superior to the accuracy of any single background observation. This is a key property which reduces the variance $\sigma^2(I)$ from $I + (1 + \gamma^2)B$ to I. For clarity and brevity, we will illustrate our point *via* a numerical example. The background model is based on $\sum B(H)$. Let that sum be equal to 10^5 counts. At the Bragg position H, the model predicts *via* (4) a local background of 100 counts. To go from the model to the expected local background, we have to divide the model signal 10^5 by 10^3. If the signal is divided by 10^3, then the variance goes down by 10^{-6}. So, the expected background becomes 100 ± 0.3 counts and the predicted background is almost error free.

Let us now look again at the calculation of the net intensity I. Since the coherent Bragg intensity I and the local background B are unrelated, the raw intensity R is given by $P(R) = P(I)P(B)$. $P(R)$ is known *via* the observation R. $P(B)$ is, given our equipment, a counting statistical distribution, which for backgrounds >30 counts can be written in the Gaussian form $\exp[-(B - b)^2/2b]$. Here b is inferred from the background model. To obtain $\langle I \rangle$ and $\sigma^2(I)$, we need to evaluate the first and second moments of $P(I)$, which is equal to $P(R)/P(B)$. This leads to

$$I = R - b \tag{5a}$$

$$\sigma^2(I) \simeq I. \tag{5b}$$

In contrast to (1b), we find a variance $\sigma^2(I)$ that is practically independent of the background. This difference is logical because the background model defines an accurate zero level upon which the Bragg intensities are superimposed as separate and independent signals.

The practical detection limit of diffractometer data is related to $\sigma(I)$. This suffices to show that the presence of a background model lowers this practical limit by a magnitude. This opportunity should be exploited in protein crystallography as well as in the study of intermolecular interactions, which depends on intensity data measured above 1 Å^{-1}.

So far, we looked at calculated backgrounds to be subtracted from a measured signal R. Such a procedure can be exploited during data collection in order to identify local anomalies (diffuse scattering, incommensurate intensity signals). Another logical development would be to include the background model in the structure refinement, because it allows the direct use of the real observation $R(H)$.

In a previous paper (Lenstra, Verbruggen *et al.*, 1991), we have illustrated the application of background modelling *via* the analysis of a diketopiperazine structure $C_{11}H_{18}N_2O_2$. To complete the information on random error analysis, we also refer to a previous paper of Lenstra *et al.* (1998). Here we have shown that an additional reduction in $\sigma^2(I)$ is possible *via* a modification in the measuring strategy. In this paper, we have $\sigma^2(I) = I$. Using a time series of fast step-scan measurements, the variance $\sigma^2(I)$ can easily be reduced to $I/5$ *via* Bayesian statistics.

References

Ahmed, F. R. (1969). Editor. *Crystallographic Computing*, pp. 255–296. Copenhagen: Munksgaard.

Amorós, J. L. & Amorós, M. (1968). *Molecular Crystals: their Transforms and Diffuse Scattering*. New York/London/Sydney: John Wiley.

Arnt, U. W. & Wonacott, A. J. (1977). Editors. *The Rotation Method in Crystallography*. Amsterdam: North Holland.

Blessing, R. H. (1989). *J. Appl. Cryst.* **22**, 396–397.

Eisenstein, M. & Hirshfeld, F. L. (1983). *Acta Cryst.* **B39**, 61–75.

French, S. & Wilson, K. (1978). *Acta Cryst.* **A34**, 517–525.

International Tables for X-ray Crystallography (1967). Vol. II. Birmingham: Kynoch Press.

International Tables for X-ray Crystallography (1968). Vol. III. Birmingham: Kynoch Press.

James, R. W. (1967). *The Optical Principles of the Diffraction of X-rays*. London: Bell.

Lehmann, M. S. & Larsen, F. K. (1974). *Acta Cryst.* **A30**, 580–584.

Lenstra, A. T. H., Bracke, B., van Dijk, B., Maes, S., Vanhulle, C. & Desseyn, H. O. (1998). *Acta Cryst.* Submitted.

Lenstra, A. T. H., Geise, H. J. & Vanhouteghem, F. (1991). *Acta Cryst.* **A47**, 567–604.

Lenstra, A. T. H., Verbruggen, M., Bracke, B., Vanhouteghem, F., Reyniers, F. & Borremans, F. (1991). *Acta Cryst.* **B47**, 92–97.

Maes, S., Lenstra, A. T. H., Slootmaekers, B. & Desseyn, H. O. (1998). In preparation.

Navaza, J. (1991). In *Crystallographic Computing 5*, edited by D. Moras, A. D. Podjarny & J. C. Thierry. Oxford University Press.

Vries, R. Y. de, Briels, W. J. & Feil, D. (1994). *Acta Cryst.* **A50**, 383–391.

Willis, B. T. M. & Pryor, A. W. (1975). *Thermal Vibrations in Crystallography*. Cambridge University Press.

Wooster, W. A. (1962). *Diffuse X-ray Reflections from Crystals*. Oxford University Press